

Feasibility study of a single-shot 3D electron bunch shape monitor with an electro-optic sampling technique

Yuichi Okayasu,* Hiromitsu Tomizawa, Shinichi Matsubara, and Noritaka Kumagai
JASRI, 1-1-1 Kouto, Sayo-cho, Sayo-gun, Hyogo 679-5198, Japan

Akira Maekawa and Mitsuru Uesaka

Nuclear Professional School, University of Tokyo, 2-22 Shirakata-Shirane, Tokai, Naka, Ibaraki, 319-1188, Japan

Tetsuya Ishikawa

RIKEN, 1-1-1 Kouto, Sayo-cho, Sayo-gun, Hyogo 679-5198, Japan

(Received 1 September 2011; revised manuscript received 28 December 2012; published 21 May 2013)

We developed a three-dimensional electron bunch charge distribution (3D-BCD) monitor with single-shot detection, and a spectral decoding based electro-optic (EO) sampling technique for a nondestructive monitor enables real-time reconstruction of the three-dimensional distribution of a bunch charge. We realized three goals by simultaneously probing a number of Pockels EO crystals that surround the electron beam axis with hollow and radial polarized laser pulses. First, we performed a feasibility test as a simple case of a 3D-BCD monitor probing two ZnTe crystals as EO detectors installed on the opposite angle to the electron beam axis and confirmed that we simultaneously obtained both EO signals. Since the adopted hollow probe laser pulse is not only radially polarized but also temporally shifted azimuthally, some disorders in the radial polarization distribution of such a laser pulse were numerically analyzed with a plane-wave expansion method. Based on the above investigations, the 3D-BCD monitor is feasible both in experimental and numerical estimations. Furthermore, we previously developed a femtosecond response organic crystal as a Pockels EO detector and a broadband probe laser (≥ 350 nm in FWHM); the 3D-BCD monitor realizes 30- to 40-fs (FWHM) temporal resolution. Eventually, the monitor is expected to be equipped in such advanced accelerators as XFEL to measure and adjust the electron bunch charge distribution in real time. The 3D-BCD measurement works as a critical tool to provide feedback to seeded FELs.

DOI: [10.1103/PhysRevSTAB.16.052801](https://doi.org/10.1103/PhysRevSTAB.16.052801)

PACS numbers: 41.75.Ht, 42.55.Tv, 42.60.Jf

I. INTRODUCTION

In x-ray free electron laser (XFEL) accelerators, we must measure a few tens of femtoseconds (FWHM) of electron bunches with a nondestructive method [1–3]. Moreover, both longitudinal and transverse simultaneous detection, i.e., 3D-BCD detection, are required to realize precise measurements for such an ultrashort electron bunch. So far, measurement with an rf deflector [4,5] has been adopted to measure the temporal distribution of such electron bunches, for example, in SPring-8 angstrom compact free electron laser (SACLA) [5]. Since this measurement is destructive, it cannot be used during user operation with self-amplified spontaneous emission (SASE) generation; another diagnostics system with a nondestructive measurement is required. The typical bunch size of XFEL is ~ 100 μm (rms) for the transverse and ~ 30 fs

(FWHM) for the longitudinal direction; the aspect ratio is estimated to be $\sim 1:10$. Thus, the bunch size must be three-dimensionally evaluated for precise measurements. For higher harmonic (HH)-seeded FELs, both the HH pulse and the electron bunch must be three-dimensionally overlapped at all times. Therefore, 3D-BCD measurements with a probe laser, which is branched from the HH-drive laser pulse, are necessary to keep the optimal overlapping between HH pulse and electron bunch at the entrance of the undulator section.

One candidate for such a monitor is electro-optic (EO) sampling-based bunch duration measurements [6]. In this method, the Coulomb field distribution of a relativistic electron bunch is encoded onto a probe laser pulse by polarization retardation by the EO effect. Single-shot measurement is also realized with a linear-chirped probe pulse (spectral decoding) [7]. In the manner of spectral decoding, the phase of each spectral component of a linear-chirped probe pulse is retarded when the terahertz (THz) field from an electron bunch and the probe pulse copropagate inside the EO crystal. This polarization retardation is converted to an intensity modulation of the spectrum at a polarizer. Thus, the temporal distribution of the electron charge

*okayasu@spring8.or.jp

Published by the American Physical Society under the terms of the Creative Commons Attribution 3.0 License. Further distribution of this work must maintain attribution to the author(s) and the published article's title, journal citation, and DOI.

density in an electron bunch can be obtained by spectral intensity modulation measurements of the encoded probe pulse.

The temporal resolution of spectral decoding is mainly limited by the following four factors: (1) restriction from Fourier transform limitation and a chirped pulse width of a realistic probe laser; (2) dispersion (refractive indices) of the EO crystal depends on crystal thickness and frequency domain (both optical and THz regions); (3) distance from the electron beam axis and electron bunch energy; and (4) velocity mismatch between the probe laser pulse in the EO crystal and the electron bunch in a vacuum.

First, we express the limitation of the temporal resolution (T_{res} in FWHM) in the spectral decoding due to the Fourier transform limitation and the chirped pulse width of a realistic probe laser [7] as

$$T_{\text{res}} \approx \sqrt{\tau_0 \tau_c}, \quad (1)$$

where τ_0 (FWHM) is the pulse width of a Fourier transform limited pulse and τ_c (FWHM) the chirped pulse width of an EO probe laser.

The second reflects the spectral dispersion in the optical (probe laser pulse) and THz regions (electric field of an electron bunch). The transient electric field is equivalent to a half-cycle of a THz pulse that impinges on the EO crystal, when a relativistic electron bunch passes within a few mm of the crystal [8]. The dispersion in the THz region especially limits the femtosecond temporal resolution. A THz temporal pulse is distorted and broadened inside the EO crystal.

The third is a geometrical limitation (T_{geo} in FWHM). Since the electric field of the relativistic electron bunch has an opening angle of $2/\gamma$, the resolution is defined as $T_{\text{geo}} = r/\gamma c$, where γ is the Lorentz factor and r is the distance between the electron bunch axis and the probing point at the EO crystal [8].

The last factor reflects the velocity mismatch between the electric field of the electron bunch in a vacuum and the probe laser pulse inside the EO crystal. Since the refractive indices of the EO crystals, especially the Pockels EO crystals, are generally as high as ~ 2 , which is almost half the speed of light in a vacuum, thinner crystals achieve better temporal resolution. The crystal thickness, which determines the polarization retardation, must be optimized by referring to the S/N ratio of the EO signal.

In addition to the electron bunch length evaluation, we must also monitor the transverse charge density distributions of the electron bunches, for example, in SACLA operations. In fact, an electron bunch should be guided in a straight line at an undulator section with a pointing stability less than $10 \mu\text{m}$ in SACLA. Although many rf-beam position monitors (BPMs) with less than $1 \mu\text{m}$ (rms) resolution and screen monitors with $2.5 \mu\text{m}$ (rms) resolution have been successfully developed for SACLA [9], single-shot measurements with real-time

reconstruction of bunch charge distribution, which can simultaneously measure both longitudinal (temporal) and transverse (spatial) bunch charge distributions (3D-BCD), enable fine optimization of electron BCD and energy chirping conditions during SACLA operation. At the undulator section, the electron beam halo is suppressed to avoid radiation damage to the permanent magnets, especially of the in-vacuum undulators; this is also a favorable condition for our EO sampling system. Such a 3D-BCD monitor has two main advantages for which spectral decoding is a unique technique rather than temporal or spatial decoding. First, it can detect a transverse charge distribution of the lasing slice. Such sliced distribution is essential for x-ray lasing instead of projected distribution. Second, the transverse beam size ($40 \mu\text{m}$ in rms) is larger than the longitudinal one (30 fs in FWHM, corresponding to $10 \mu\text{m}$ in the scale) in SACLA. In this case, a slight tilt of the beam trajectory can disturb precise bunch duration measurements. With a nondestructive real-time 3D-BCD monitor, we can correct the tilt and perform precise longitudinal measurements. Eventually, fine beam tuning can be realized just before the undulator section.

Based on these above issues, we are developing our novel 3D-BCD monitor with capable 30-fs (FWHM) temporal resolution, as proposed by Tomizawa at SPring-8 in 2006 [10,11].

II. PRINCIPLE OF 3D DETECTION

A. Basic idea

The 3D-BCD monitor has the following four features: (1) nondestructive, (2) single-shot, (3) real-time reconstruction, and (4) three-dimensional detection of electron bunch charge distribution with 30-fs (FWHM) temporal resolution.

A schematic of the elements of the 3D-BCD monitor based on spectral decoding is shown in Fig. 1 (upper). Broadband ($\sim 350 \text{ nm}$ in FWHM at 800 nm) and linear-chirped probe laser pulse with a squared intensity spectrum is formed, which is essential for real-time BCD reconstruction. A hollow-shaped probe laser beam is also generated by an axicon lens or mirror pair. Then polarization of the probe laser is converted from linear to radial polarization. The electron beam perpendicularly passes through the center of the three EO detectors, in which each detector consists of eight Pockels crystals [Fig. 1 (lower)]. The three independent probe laser pulses that split from the original laser source are synchronized to probe the same electron bunch at each EO detector. At each EO crystal, the longitudinal distribution of the Coulomb field by the relativistic electron bunch is encoded as retardation on the probe laser spectra. The incident angles and the positions of the electron bunch (the center of the bunch charge slices) are determined by the set of two detectors at both ends (Pockels EO detector 1 and 3 in Fig. 1). The BCD of the

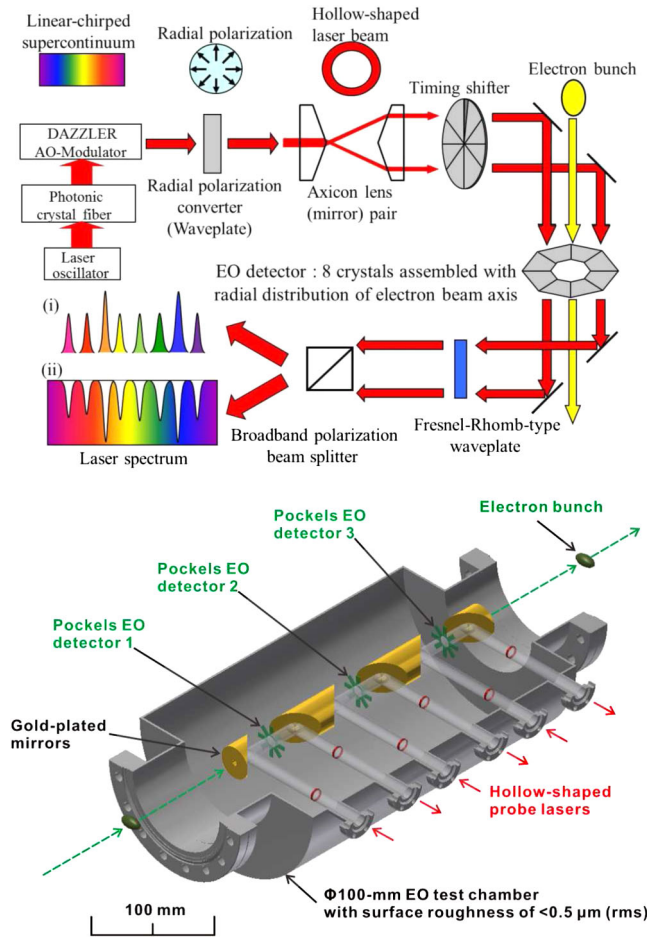


FIG. 1. Schematic of elements of 3D-BCD monitor (upper) and total system of 3D-BCD (lower).

electron bunch (transverse) and its temporal distribution (longitudinal) are measured by the three EO detectors.

The phase retardation of the probe laser pulse is divided into p - and s -waves by a polarized beam splitter (PBS) and decoded by a multichannel spectrometer that enables single-shot measurements.

The three-dimensional detection of the electron BCD is divided into the following discussions of longitudinal (temporal) and transverse (spatial) detection.

B. Longitudinal detection

The longitudinal detection of the electron bunch charge distribution requires less than 40-fs (FWHM) temporal resolution (Sec. I). To achieve this goal, the following issues are crucial: (1) a broadband and linear-chirped probe laser generation and (2) the spectral transmission characteristics of Pockels EO crystals.

First, we prepare a broadband square intensity spectrum (~ 350 nm in FWHM at 800 nm of central wavelength) probe laser pulse in which $\tau_0 \approx 3$ fs (FWHM). During EO sampling with a single Pockels EO crystal, $T_{\text{res}} \approx 30$ fs (FWHM) is easily achieved with a $\tau_c \approx 300$ –400 fs

(FWHM) linear-chirped probe laser pulse based on Eq. (1). Indeed, eight Pockels EO crystals should be probed without any spectral region overlap of each other in the 3D-BCD monitor. When the arrival timing jitter between the probe laser pulse and the electron bunch is 50 fs (FWHM), $\tau_c \approx 600$ fs of linear-chirped probe pulse is required, and $T_{\text{res}} \approx 40$ fs (FWHM) is expected.

Second, the following spectral transmission characteristics, which limit the temporal resolution of the Pockels EO crystals, must be examined: (1) absorption in the THz range, (2) velocity mismatch inside the crystal media between the THz and probe laser pulses, and (3) dispersion of the crystal media in an optical wavelength range in addition to the THz range. Using ZnTe or GaP for bunch duration measurements, which have generally been adopted as inorganic Pockels EO crystals, their temporal resolutions are limited to ~ 90 fs (rms) in ZnTe and ~ 50 fs (rms) in GaP with appropriate thickness because they have photon absorption around 5 and 11 THz, respectively [8,12]. Thus, the Coulomb field is distorted to propagate in such crystals. To achieve the targeted temporal resolution, the Pockels EO crystals should be transparent in a wide frequency range. Therefore, we introduce organic Pockels EO crystals to overcome this issue.

Contribution of the geometrical limitation T_{geo} is negligible. Since the Pockels EO crystal is generally placed 0.5–2 mm apart from the electron bunch to avoid their interference, T_{geo} is estimated to be less than sub-fs (FWHM) in case of 8 GeV electron bunch energy.

The details and a comparison discussion of the Pockels EO crystals and other candidates are discussed in Sec. III B.

C. Transverse detection

Detecting the transverse distribution of the electron bunch charge density is equivalent to identifying the mass center, i.e., the moment of the temporally sliced BCD. Figure 2 explains the principles. For example, for BCD detection with two EO crystals, the mass center of the sliced BCD is only defined at one point as $(I_1 + I_2)/2$ (I_n is signal intensity of the n th EO crystal). For four crystals, which are the coordinates of the mass center, the first order of the moment of the BCD on the sliced plane can be defined with $(I_1 + I_3)/2$ and $(I_2 + I_4)/2$. BCD measurement with eight EO crystals, which we propose, defines the third order of the moment on the sliced plane. Eventually, 3D-BCD measurements enable not only precise temporal detection but also spatial BCD detection of temporally sliced BCD with a higher order of moment.

To evaluate its feasibility, the intensity modulation is estimated for eight Pockels EO crystals at each detection point. In the calculations, the electron beam energy is 8 GeV, the bunch charge is 100 pC, and the longitudinal charge distribution is assumed to be a Gaussian distribution

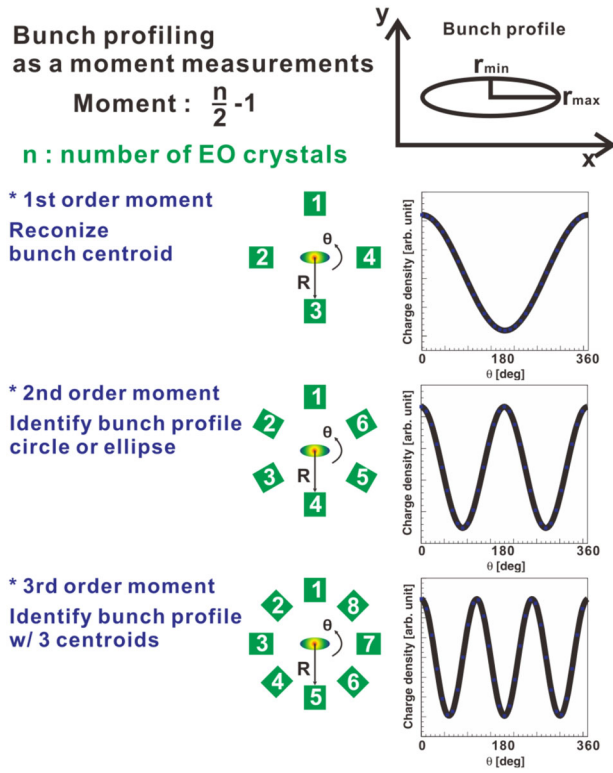


FIG. 2. Transverse bunch profiling as moment measurements.

with 30-fs (FWHM), based on SACLA parameters. To detect the transverse distribution, the detection points should be close to the beam axis, as discussed in Sec. I. Here, we assume that the detection points are set at $r = 2$ mm. The calculation results are presented in Fig. 3 when (a) the beam center (beam size of $40 \mu\text{m}$ in rms) shifts $10 \mu\text{m}$ away from the center of the EO crystals (Sec. I), and (b) the transverse charge distribution becomes ellipse shaped (aspect ratio is $r_{\text{hol}}:r_{\text{ver}} = 2:1$, $\sqrt{r_{\text{hol}} \cdot r_{\text{ver}}} = \sqrt{2} \times 40 \mu\text{m} \approx 60 \mu\text{m}$, where r_{hol} and r_{ver} are the horizontal and vertical beam size in rms, respectively).

At $r = 2$ mm, the electric field of the electron bunch is evaluated to be ~ 100 MV/m at maximum by Eq. (2):

$$E(r) = \frac{Q}{(2\pi)^{3/2} \epsilon_0 c r \sigma_b}, \quad (2)$$

where Q is the bunch charge, c is the light velocity, and σ_b is the bunch length in sigma. In the case of isotropic EO crystals, the change in the refractive index (Δn) of the EO media is expressed as a function of $E(r)$:

$$|\Delta n| = \frac{n_0^3}{2} \{ \xi_p E(r) + \xi_k E^2(r) \}. \quad (3)$$

In the right-hand side of Eq. (3), the linear term represents the Pockels EO and quadratic term Kerr EO effects. n_0 is a refractive index of the EO medium. ξ_p and ξ_k are Pockels and Kerr EO coefficients, respectively. The Kerr EO effect

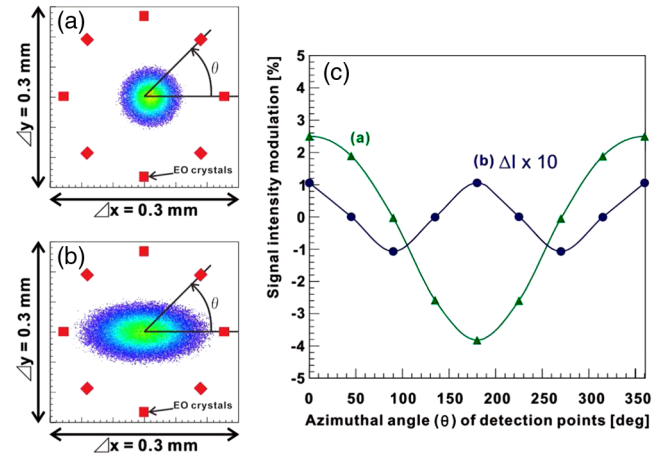


FIG. 3. Calculation results of azimuthal intensity modulation of EO signals. Calculated conditions (a) $10 \mu\text{m}$ transverse shift of electron beam with beam size of $40 \mu\text{m}$ (rms) and (b) ellipse-shaped sliced profile with a beam size of $150 \mu\text{m}$ (rms). Bunch charge and duration are assumed to be 100 pC and 30 fs (FWHM), respectively. 1 mm thick of ZnTe is adopted as the Pockels EO crystal. The relative position of EO crystals and definition of azimuthal angle ($0 < \theta$ [deg] $< 2\pi$) of the detection point are overlaid. Intensity modulations for both (a) and (b) are compared in (c).

can be found in any EO material, but there is no Pockels EO effect in EO materials where the crystal structure has a point symmetry. In general, the Kerr EO effect is known to be weak and negligible compared to the Pockels EO effect, especially in a low electric field.

In such a strong field (~ 100 MV/m), the EO effect is expressed to observe not only the Pockels effect but also the Kerr effect. EO sampling with amorphous Kerr EO material may realize precise BCD measurements with a background-free spectra, i.e., a higher extinction ratio. The details will be discussed in Sec. III B.

Here, we adopt 1 mm thick of ZnTe, Pockels EO crystal, $n_0 = 2.85$ of the refractive index [13] and $\xi_p = 3.97 \times 10^{-12}$ m/V of the Pockels EO coefficient for the calculation. No contribution of the Kerr effect is involved in the calculation.

Figure 3(c) represents the azimuthal intensity modulation of the EO signals at the detection points. Intensity modulation ΔI is defined as

$$\Delta I = \frac{I_{\text{sig}} - I_{\text{org}}}{I_{\text{org}}}, \quad (4)$$

where I_{org} is the EO signal intensity without the transverse shift of the electron beam and I_{sig} can be calculated for different experimental configurations:

$$I_{\text{sig}} = I_0 \sin^2\left(\frac{\pi}{2\lambda} \Delta n L\right) = I_0 \sin^2\left(\frac{\pi n_0^3 \xi_p E L}{4\lambda}\right). \quad (5)$$

TABLE I. Optical components for super continuum laser pulse: 650–1100 nm.

Item	Wavelength range
Radial polarization converter (nematic liquid crystal)	350–1700 nm
DAST crystal	Transparent in 600–2000 nm [14]
Fresnel-Rhomb wave plate	$T \geq 95\%$ in 600–1100 nm
Polarizing beam splitter	$T_p \geq 90\%$ in 600–1100 nm
Antireflection coating	$R \leq 0.5\%$ in 600–1100 nm
Quartz glass (transparent optics)	$GVD \leq 60 \text{ fs}^2/\text{mm}$ in 600–1100 nm
Al mirror	$R \geq 80\%$ for $\geq 600 \text{ nm}$
DAZZLER (UWB-650-1100)	Adjustable up to the 7th order dispersion and intensity spectrum shaping in 650–1100 nm

Here, we assume wavelength (λ) of the probe laser pulse as 800 nm and 1 mm thick (L) of ZnTe crystal for the calculations, and I_0 is treated as 1. In the case of Figs. 3(a) and 3(c), $\sim 6\%$ of the intensity modulation difference is expected to be induced in ZnTe, which can be detected in actual experiments. On the other hand, in Figs. 3(b) and 3(c), $\sim 0.2\%$ of the quite weak intensity modulation difference is expected even for $\geq 150 \mu\text{m}$ of beam size. In SACLA, the ellipse-shaped beam size is $\sim 40 \mu\text{m}$; thus detecting the transverse-BCD asymmetry of the electron bunch is difficult with the above criterion. For such a relatively small intensity modulation, we measure an s -wave spectrum instead of a p -wave one for a higher S/N ratio, i.e., an extinction ratio, as described in Fig. 1 (upper).

III. REALIZATION

A. Broadband optical components for probe lasers

In this section, we introduce and discuss individual optical components that comprise the 3D-BCD monitor. The primary optical components adopted in the 3D-BCD monitor system are listed in Table I. We prepared these broadband optical components for a ~ 30 -fs temporal response EO crystal like DAST (4- N , N -dimethylamino-4'- N' -methyl stilbazolium tosylate) [15], not for ZnTe or GaP, which is discussed in Sec. III B.

The 0th order of the diffracted IR (the fundamental wavelength) at the compressor gratings of the Ti:sapphire laser system is used for photocathode illumination. To generate a probe pulse with a broadband, linear-chirped, and square intensity spectrum, we follow these three steps [16]: (1) broadening the spectral bandwidth of a seed laser pulse with a photonic crystal fiber (PCF); (2) single-pass amplification with broadband phase matching by noncollinear optical parametric amplifiers (NOPAs); (3) shaping a square intensity spectrum and controlling the phase spectrum to make it linear chirped with a broadband acousto-optic (AO) modulator.

A Ti:sapphire laser (800 nm, $\leq 100 \text{ mW}$, and 89.25 MHz) is injected to a PCF (SCG-800, Newport) [17], and its output ($\sim 0.1 \text{ nJ}$) is amplified to $\sim 100 \mu\text{J}$

by double NOPA stages with the second harmonic generation (SHG, 395 nm) of the original pulse as the 1st stage and SHG of a Yb:YLF laser (510 nm) as the 2nd stage. In addition, the probe laser spectrum is square shaped by a broadband AO modulator, DAZZLER (UWB-650-1100, FASTLITE) [18], which is located between the 1st and 2nd NOPA stages [Fig. 4 (upper)].

We performed a feasibility test by combining PCF and broadband DAZZLER, as described in Fig. 4 (lower). We obtained flattop intensity distribution in the 250-nm bandwidth with $\sim 300 \text{ nm}$ (FWHM) of the probe laser. We expect that a square-shaped ~ 350 -nm bandwidth spectrum is realized with the two-stage NOPA system to compensate for the broadband DAZZLER.

For the transverse detection, a radially polarized and hollow-shaped laser pulse is required as the EO probe laser in the 3D-BCD monitor. To generate a radially polarized laser beam from a linearly polarized source, several methods have been studied, including an interfered method [19] and methods using a liquid crystal (twisted nematic effect) [20,21] and a divided wave plate [11]. Among these techniques, the liquid-crystal-based method satisfies the broad bandwidth, as described in Table I. Therefore, it is favorable for our 3D-BCD monitor with a broadband ($\geq 350 \text{ nm}$) probe laser pulse to achieve 30 fs (FWHM)

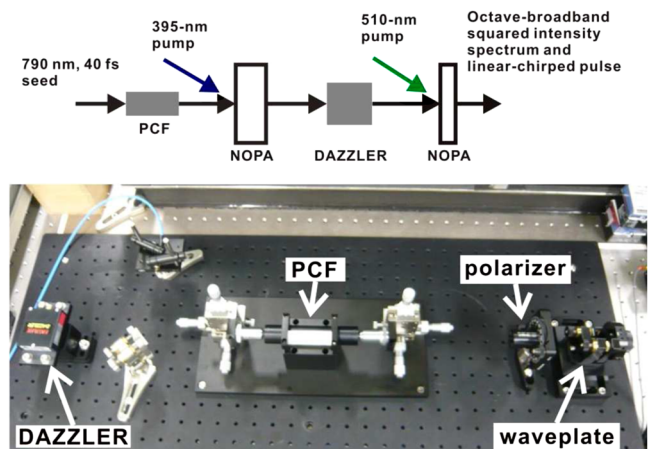


FIG. 4. Broadband probe laser generation.

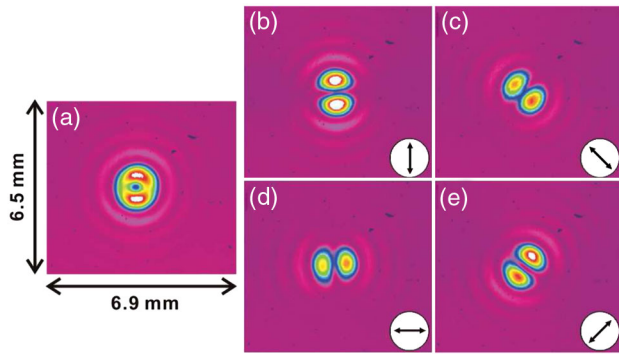


FIG. 5. Beam profiles after a spatial filter unit without (a) and with (b)–(e) a polarizer. Arrows represent polarization directions. TEM₀₁ and TEM₁₀ modes appear through the linear polarizer, indicating that radial polarization is generated with a nematic-liquid-crystal radial polarization converter.

of realistic temporal resolution. Figure 5 shows the obtained images after the polarization is converted by a nematic-liquid-crystal radial polarization converter with a spatial filter unit. This radially polarized laser is injected into an axicon lens or a mirror pair unit to generate a hollow-shaped laser.

The obtained images of a radially polarized hollow laser beam are shown in Fig. 6. The ring width of the hollow laser beam is determined by the incident laser beam size at the first axicon lens's vertex. The hollow beam's outer diameter is controlled by changing the distance between the two axicon lenses. We also measured the probe laser pulse, which propagates through eight Pockels EO crystals, as intensity modulation in a spectrum with a multichannel spectrometer by eight-branched optical fibers. To probe each EO crystal with a single probe laser, we installed a timing shifter that consists of eight different optical glasses

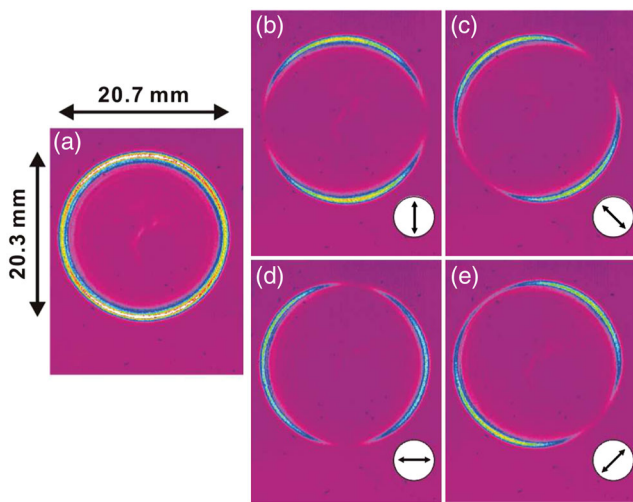


FIG. 6. Radially polarized laser with anti-Gaussian profile (hollow beam) after axicon lens pair without (a) and with (b)–(e) polarizers. Arrows represent polarization directions.

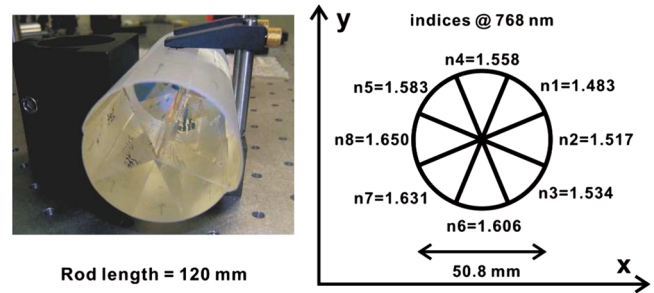


FIG. 7. Eight-divided optical glasses (left). Individual refractive index (incident wavelength: 768 nm) is described in the schematic drawing (right).

(n₁: S-FSL5; n₂: S-NSL5; n₃: S-BAL12; n₄: S-BAL41; n₅: S-BAL35; n₆: S-BSM18; n₇: S-BSM18; and n₈: S-BSM25) with different refractive indices. The corresponding spectral regions for each EO crystal are temporally shifted to each other without temporal overlapping. Figure 7 shows a prototype of a 120-mm long timing shifter for a feasibility test in the advanced photocathode test facility at SPring-8 described in III C and IV. At this facility, since we measure electron beams with a 10-ps (FWHM) bunch length, the timing shifter must exceed 10-ps temporal shifts between neighboring optical glasses. In the case of 30-fs (FWHM) bunch length detection with a ~ 100 fs temporal shift, we can reduce the rod length to a few millimeters.

B. Novel EO materials

As already discussed in Sec. II A, organic Pockels EO crystals are introduced for THz detection in the 3D-BCD monitor. Compared with inorganic Pockels EO crystals, organic ones have higher temporal response due to the existing π -bonding electrons [22], which means that the material is available for a broad spectral range. DAST is one promising candidate for an organic Pockels EO crystal because it has a large Pockels coefficient of $r_{111} = 77 \pm 8$ pm/V at 800 nm and is transparent at 699–2000 nm [14]. Since the electron bunch with Gaussian distribution of 30-fs (FWHM) bunch length has frequency components up to 30 THz, the Pockels EO crystal must have no anomalous dispersion and a low absorption coefficient in this spectral region. THz wave generation in 2–31.5 THz with DAST crystal has been reported, which verifies the feasibility of DAST in this spectral region [23]. A feasibility examination of the BCD measurements with a single DAST crystal was successfully demonstrated on February 2012 at the EUV-FEL accelerator, SPring-8. Experimental conditions for electron bunches, probe laser pulses, and the Pockels crystals are listed in Table II. As described in Table II, since total volume of the DAST crystal is much smaller and average driving pressure of the accelerator is 5×10^{-6} Pa, outgassing of the DAST crystal is negligible. Replacement of the DAST crystal can be handled as ZnTe. No special

TABLE II. Experimental conditions at the EUV-FEL accelerator, SPring-8.

Electron bunch	
Energy	250 MeV
Bunch charge	~300 pC
Bunch duration	~300 fs (FWHM)
Repetition rate	30 Hz
Peak current	>300 A
Probe laser pulse	
Bandwidth	5 nm (FWHM) @ 795 nm
Pulse energy	5 μ J (40 μ J/cm ²)
Pulse duration	5 ps (FWHM)
Linear chirp rate	0.6 ps/nm
Repetition rate	30 Hz
EO crystals	
DAST	2 ^W × 3 ^D × 0.23 ^H mm ³
ZnTe	3 ^W × 4 ^D × 1 ^H mm ³

process is required such as differential evacuation. The measured EO signal spectrum with the DAST crystal is shown and compared with the spectrum via a ZnTe crystal in Fig. 8. The EO signal spectrum with the DAST crystal shows fast temporal response compared to that with the ZnTe crystal in Fig. 8. During the feasibility experiment, the EO signal with the DAST crystal was gradually decreased and survived for ~40 minutes. Our recent investigation results show that this phenomenon is caused by the radiation dose which is radiated by an optical transition radiation monitor installed 0.5 m upstream from the BCD monitor chamber. This radiation damage of the DAST crystal can be avoided by controlling the integrated spatial radiation dose near the chamber not to exceed ~100 Gy.

On the other hand, as discussed in IIC, the Kerr EO effect cannot be negligible in ~100 MV/m of a strong electric field. For example, for the condition with ZnTe that was previously described IIC, signal intensity associated with the Kerr EO effect is estimated to be 40%–70% of that with the Pockels EO effect [Fig. 3(b)]. Such amorphous Kerr EO materials as polymethyl methacrylate [24] can be effective candidates for such strong fields since they only have an even order of EO effects (the Kerr effect is the lowest order and the dominant EO effect in the materials) [25], they can minimize the background noise induced by wakefields and so on. Kerr EO detection with amorphous Kerr EO media enables high contrast, background-free measurements [26].

C. Numerical feasibility study for optical setup

High signal-to-noise EO measurements with spectral decoding require precise polarization control with high extinction ratios in the Cross-Nicole condition. As discussed above, we have various optical components in our experimental setup, and the generated probe pulse must be radially polarized and hollow. Therefore, polarization

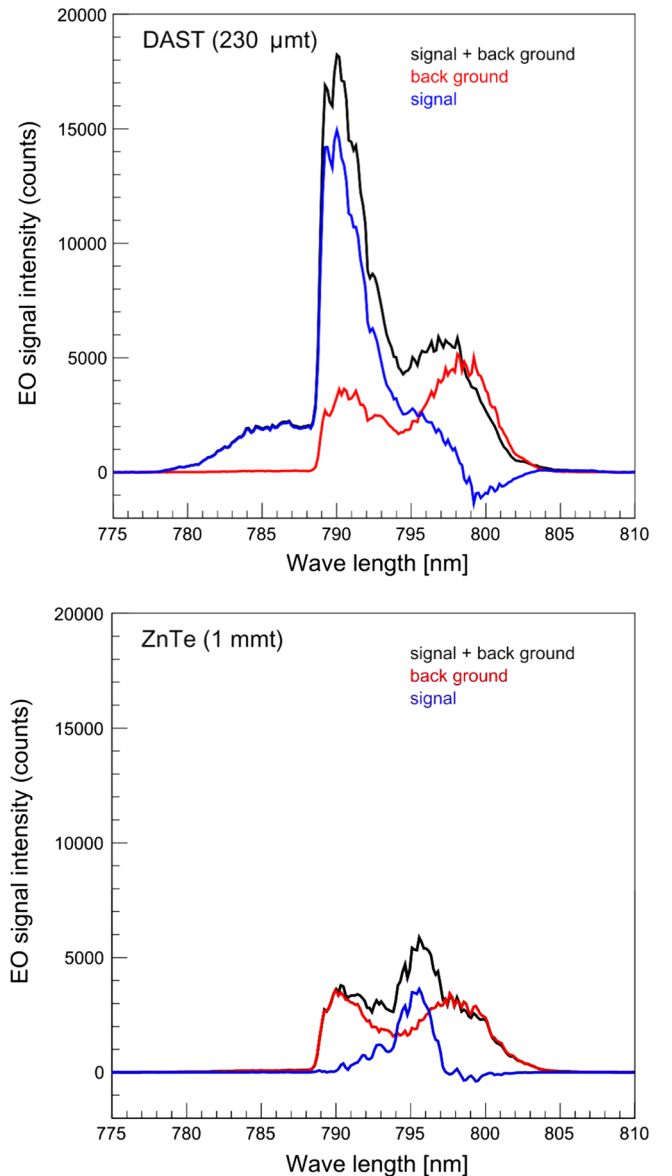


FIG. 8. Measured EO signal spectra with DAST (upper) and ZnTe (lower) crystals. For each figure, the original signal and background spectra measured by Ocean Optics, QE65000 spectrometer are described as black and red, respectively. Blue curves are subtraction between signal and background spectra.

control for the probe pulse is essential to improve the extinction ratio. Numerical analysis of polarization propagation is demonstrated with a commercial program called VirtualLabTM [27] that integrates an actual experimental setup for the feasibility test and gives appropriate feedback to optical component designs, if necessary.

In this program, the probe pulse's field propagation is defined in two categories: propagation in free fields and optical component media. For free space propagation, we adopted the plane-wave expansion method for short range propagation and treated long range calculation as a Fresnel diffraction determined by the Nyquist theorem in a

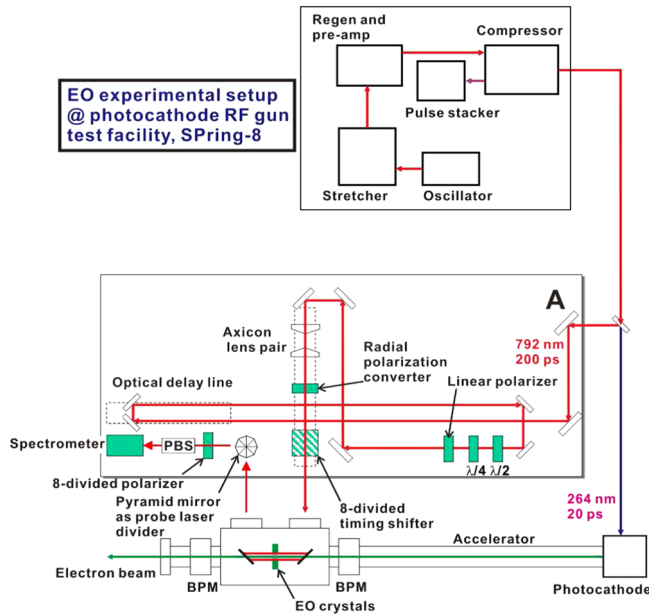


FIG. 9. Experimental apparatus for a 3D-BCD monitor feasibility test at the photocathode rf gun test facility, SPring-8.

sampling boundary region [28]. Optical components are generally described as the multiplication of field amplitude, phase transition, and polarization rotation functions. Indeed, the field propagations in the axicon lens pair and the timing shifter are calculated with raytracing and beam propagation methods, respectively. Figure 9 shows the actual experimental setup for the 3D-BCD monitor feasibility test at the photocathode rf gun test facility at SPring-8. The primary parameters of the electron beam and probe laser pulse source are listed in Table III and Sec. IV. The electron beam is accelerated to 25 MeV, passes through the EO sampling vacuum chamber, and is sent to a beam dumper. The electron beam's coordinates and temporal information are monitored by two BPMs located at both ends of the chamber. The probe pulse is hollow shaped ($\phi 8$ mm with a 1-mm ring width in FWHM) by the axicon lens pair, and its polarization is converted from linear to radial by the radial polarization converter [Fig. 11 (left)]. After passing through the

TABLE III. Primary parameters of electron beam and probe laser pulse source at the photocathode rf gun test facility.

Electron beam	
Energy	25 MeV
Bunch length	6–10 ps (FWHM)
Charge	~ 1.5 nC
Probe laser pulse source	
Bandwidth	20 nm (FWHM) @ 785 nm
Pulse width	200 ps (FWHM)
Beam diameter	$\phi 2$ mm (FWHM)
Pulse energy	~ 2 mJ/pulse

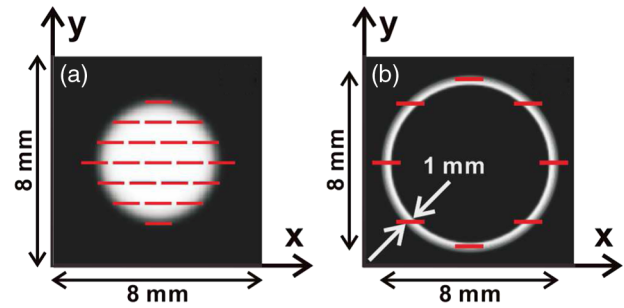


FIG. 10. Calculated laser intensity $|E(t)|^2$ distributions of probe laser before (a) and after (b) hollow shaping on the xy plane and polarization directions (fields oscillation direction) are overlaid with red lines.

eight-segmented timing shifter (Fig. 7), the probe pulse is delivered to the eight Pockels EO crystals that are arranged equally surrounding the electron beam axis.

The arrival timing of the electron beam and the probe pulse at the Pockels EO crystals are well adjusted by an optical delay line located between the axicon lens pair and the radial polarization converter (Fig. 9).

First, the original source of the linear-chirped probe laser with 20-nm bandwidth is prepared to satisfy the characteristics listed in Table III [Fig. 10 (left)]. In the analysis of polarization propagation, the probe laser source is located at a dielectric mirror marked “A” in Fig. 9.

Next, the probe pulse is propagated through a 22-m long free space, which is treated as a Fresnel diffraction in the simulation, wave plates, and a polarizer with functional operators to adjust the polarization directions. In all the calculation processes, the free space is treated as standard atmosphere.

After propagation in the free space, the probe pulse profile is shaped as a hollow beam by the axicon lens pair. As mentioned above, eight Pockels EO crystals equally surround the electron beam axis, and each crystal end is 3 mm from the electron beam axis. Therefore, the probe pulse's beam shape should be a hollow beam with an 8-mm outer diameter and a 1-mm ring width to provide the

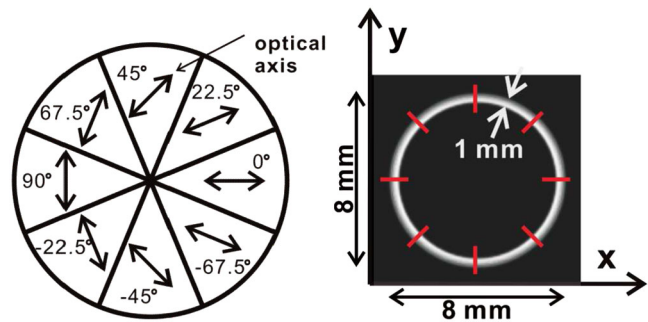


FIG. 11. Our designed model of eight-segmented half-wave-plate (left) and evaluated distribution of hollow laser intensity $|E|^2$ at the wave plate exit with polarization directions (red solid).

probe laser within a 1-mm space from each crystal end. The axicon lens pair is designed with fused silica to have a 35-mm distance between their vertices to realize such hollow-shaped parameters. Figure 10(b) represents the calculated laser intensity $|E|^2$ distribution of the hollow-shaped probe laser at the exit of the designed axicon lens pair. The polarization direction is also overlaid as red-solid lines. In the numerical calculation, we designed an eight-segmented half-wave-plate as a radial polarization converter with eight individual optical axes of the segments [Fig. 11 (left)].

The calculated laser intensity $|E|^2$ and the polarization distributions of the probe pulse are shown in Fig. 11 (right). Finally, we evaluate the effects of the timing shifter on both the fields and the polarization of the probe laser, as previously designed in Sec. III A. The 120-mm long timing shifter consists of eight optical glasses with different indices, and neighboring glasses are bounded by several optical cements with intermediate indices. Some disorders in the laser polarization will probably occur, especially around the boundary region of different optical glasses. Figure 12 represents the calculated laser intensity $|E|^2$ and the polarization distributions at the exit of the timing shifter. After propagating in the 120-mm long timing shifter, the polarization distributions are partially disordered, as shown in Fig. 12; the laser intensity distribution is not distorted. The numerical calculation suggests that such polarization disorders are localized by diffraction that is induced on the contact surfaces of different optical glasses. However, these polarization disorders can be excluded by introducing a patterned polarizer (colorPol®, CODIXX AG, Germany) that consists of eight individual polarizing axes [Fig. 12(b)] to sustain the spectral decoding EO sampling with $\geq 10^{-8}$ of ultrahigh extinction ratio at 800-nm wavelength. To estimate the disordering effect on polarization, we calculated the transition of the polarization distribution with a propagating probe laser along the optical path length. Since the probe laser's polarization should be radial in front of the EO crystals, the initial

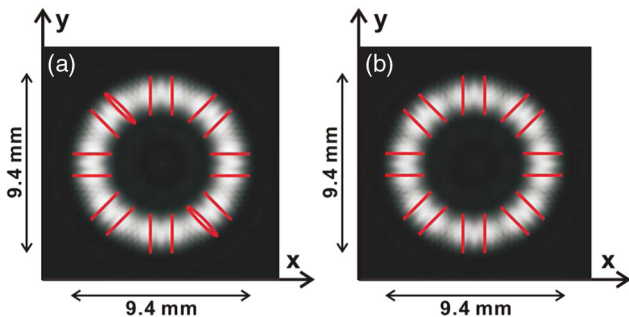


FIG. 12. Calculated distribution of hollow laser intensity $|E|^2$ and polarization (red solid) distributions of the probe laser at the exit of the designed timing shifter (a) and the patterned polarizer (b). The line and ellipse indicate linear and elliptical polarization, respectively.

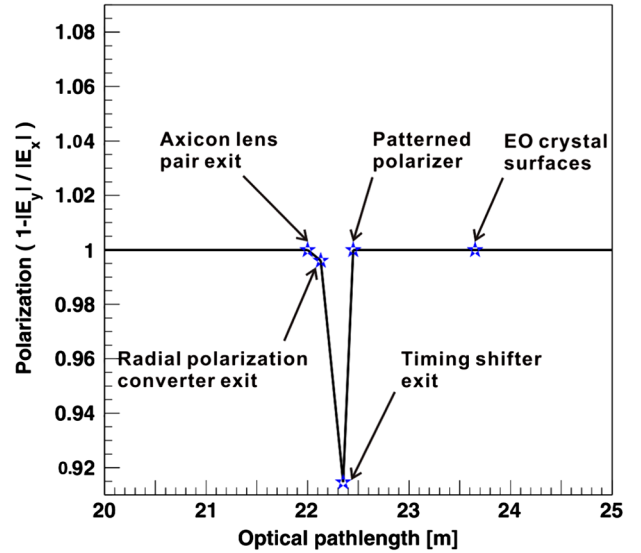


FIG. 13. Transition of polarization distribution with propagating probe laser along the optical path length. The optical path length is defined as the distance from the dielectric mirror marked “A” in Fig. 9.

polarization, which is parallel to the x axis, is conserved in some areas through the entire optical path length, such as the center of optical glasses n2 and n8 (Fig. 7). Here, we numerically selected the flux of the probe laser that passes through the $\phi 1$ mm region defined in the center of optical glass n2. The degree of change from ideal radial polarization $1 - |E_y|/|E_x|$ inside the cross sections of the flux at the exit are calculated and shown in Fig. 13 as a function of the optical path length: (1) axicon lens pair, (2) radial polarization converter, (3) timing shifter, (4) patterned polarizer, and (5) EO crystal surface. From Fig. 13, the maximum polarization disorder is evaluated as $\sim 9\%$ at the exit of the eight-divided timing shifter rod. By introducing the eight-segmented polarizer between the timing shifter and the EO crystals, the probe laser's polarization can be effectively aligned at the EO crystal surfaces.

These verifications suggest that numerical calculation of polarization propagation for the entire optical system is available. We evaluated all of the various optical components in our experimental setup and performed a feasibility experiment, as described in the next section.

IV. 3D-BCD MONITOR FEASIBILITY TEST

We performed the first feasibility test of 3D-BCD at the photocathode rf gun test facility, SPring-8 with the experimental setup described in Fig. 9.

The laser pulse (792-nm central wavelength) was divided into two. The third harmonic generation (THG) pulse (264 nm) was transported to the photocathode, and the 0th order diffraction pulse (792 nm) at the first grating of the pulse compressor was used for the EO probe pulse. The THG pulse was cylindrically shaped by the 3D laser pulse

shaping system [29], and its typical square pulse width is 20 ps (FWHM). The pulse width of the EO probe pulse was 200 ps in FWHM and linearly chirped. The laser source was distributed from the same Ti:sapphire laser system to simultaneously illuminate the photocathode in UV (THG) and probe the EO crystals in the fundamental wavelength. All require fine alignments for both the laser position and the incident angle to the axicon lens pair. A pair of Risley prisms was mounted in a pair of remote-controlled rotation stages to automatically align the laser with an advanced tactical aligner (ATA) system that is based on metaheuristic algorithms [30]. By guiding a merit function, which is calculated from laser spatial profile data, the ATA system automatically aligns a laser to the optimal path to generate a reliable hollow laser profile for the 3D-BCD monitor.

In the 3D-BCD chamber, n -Pockels EO crystals were installed azimuthally surrounding the electron beam axis for simultaneous transverse detection. This feasibility experiment was the simplest case, $n = 1$, and we adopted two 1-mm thick ZnTe ($10^W \times 10^D \times 1^H$ mm³) crystals. Note that radial polarization is required when we simultaneously probe more than eight crystals ($n \geq 3$).

The edges of both crystals were placed 3 mm from the electron beam axis. The birefringence induced by the transverse electric field of the electron bunch was probed 3 mm from the electron beam axis by the hollow probe pulse with a 1-mm ring width. The probe pulses were detected by a multichannel spectrometer with an eight-branched optical fiber. The spectrometer resolution (HR4000, Ocean Optics) was 0.2 nm in FWHM, corresponding to geometrical resolution of 1.2 ps in the temporal domain in this chirped laser probe pulse.

In the experiment's first step, a single EO signal ($n = 0$) was measured with one of the ZnTe crystals, and the measured spectra, where the signal gain becomes maximum, are shown in Fig. 14(a): The chirp linearity of the hollow probe laser pulse is measured as the wavelength shift at the EO signal peaks while changing the optical delay line (i.e., arrival timing at EO crystals) [Fig. 14(b)]. In the optical delay line, one step of a stage shifts 8 μ m ($\cong 27$ fs). The fitting result of Fig. 14(b) gives a conversion factor (chirp rate) of 9.58 ps/nm. The measured electron bunch length was 10.8 ps (FWHM) in Fig. 14(a).

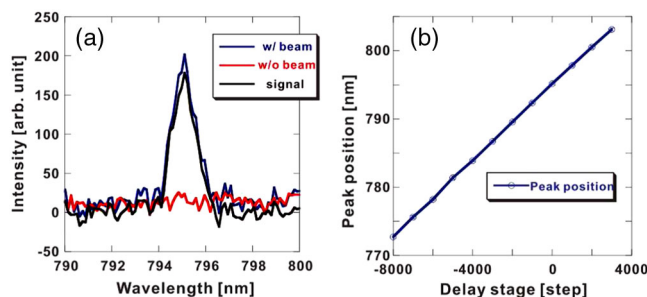


FIG. 14. Measured single EO signal (a) and chirp linearity of probe pulse (b).

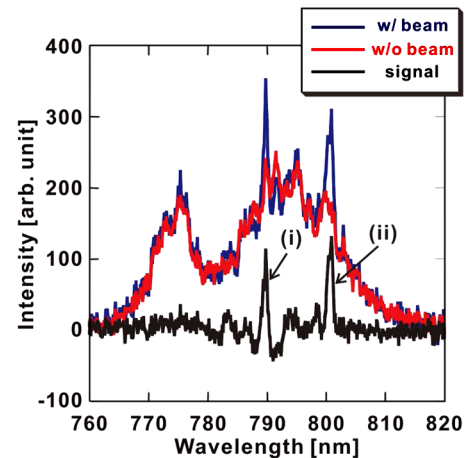


FIG. 15. Measured double EO signals with two ZnTe crystals.

In the next experiment, we installed two ZnTe crystals at opposite sides of the electron beam axis and performed a feasibility test as multiple EO detecting with a single probe beam in a 3D-BCD monitor. Double EO signals ($n = 1$) were measured simultaneously with ZnTe crystals by a probing hollow laser pulse. Two optical glasses, n2 and n8 (Fig. 7), were adopted for the timing shifts of the probe pulse, and the bunch charge was 1.3 nC. The measured spectra are shown in Fig. 15.

V. DISCUSSION

The temporal difference between the double measured peaks marked (i) and (ii) in Fig. 15 is about 110 ps, which corresponds to 11 nm. Here, we discuss the fluctuations in the EO signals in this measurement as a practical case of this monitor. The fluctuations of the peak intensities in the short period for (i) and (ii) are $\sim 13\%$ (rms), respectively. On the other hand, since the fluctuation of the peak intensity ratio (ii)/(i) is evaluated to be 13%, the fluctuation of the total bunch charge is negligible. The sum is (i) + (ii) 10%, which is considered the total laser intensity fluctuation. Eventually, the relative pointing fluctuation between the probe laser pulse and the electron bunch is estimated to be $\sqrt{(13\%)^2 - (10\%)^2} \cong 8\%$. Other possible major factors, which can induce fluctuations of the probe pulse intensity, are polarization disorders and the spectral intensity shift of the hollow laser beam. The former case is resolved by introducing the eight-divided radial polarizer, as discussed in Sec. III C; its polarization is radially aligned well. For the latter case, we introduce a thermoelectric cooled spectrometer instead of an air-cooled one by which the dark current noise is expected to be reduced by a few tens of percent.

VI. SUMMARY

We developed a nondestructive, single-shot 3D-BCD monitor with real-time reconstruction and 30-fs (FWHM)

temporal resolution. It is based on EO sampling techniques in the manner of spectral decoding. The monitor has three key parts: (1) an EO detector that consists of eight organic Pockels EO crystals azimuthally surrounding the beam axis, (2) a radially polarized and hollow probe pulse with a linear-chirped broadband square intensity spectrum, and (3) one-octave broadband optical components. With these configurations, not only longitudinal (temporal) but also transverse (spatial) bunch charge distributions are expected to be simultaneously obtained with 30-fs (FWHM) temporal resolution.

The numerical calculations for the hollow laser intensity distribution and the polarization propagation of a designed probe pulse were also advanced by our experimental setup. The calculated results suggest the availability of polarization control. We designed various optical components based on the calculations and performed a feasibility test. The calculation also shows that the polarization disorders, which are expected to be induced in the boundary region of different optical glass, can be excluded by introducing an eight-divided radial polarizer with a higher extinction ratio of $\sim 10^7$ at the wavelength region being used.

We successfully demonstrated and proved that the principle experiment of the 3D-BCD monitor is completely feasible by numerical analysis and feasibility tests. In addition, we successfully demonstrated BCD measurements with a single organic DAST crystal ($2 \text{ mm}^W \times 3 \text{ mm}^D \times 230 \mu\text{m}^H$) by the EO sampling method by changing the polarization of the hollow probe laser from radial to azimuthal. We observed higher temporal response with the DAST crystal comparing to that with an inorganic ZnTe crystal ($3 \text{ mm}^W \times 4 \text{ mm}^D \times 1 \text{ mm}^H$). This result makes a few tens of femtosecond temporal resolution in 3D-BCD measurements possible. Further optical issues such as lifetime and thermal damage [31] of the DAST crystal are investigated.

To realize a 3D-BCD monitor with 30-fs (FWHM) temporal resolution, organic Pockels EO crystals are required that provide ~ 30 -fs temporal response and light source development for probe laser pulses. Since a small percent of signal intensity fluctuation must be measured for transverse detection, the probe laser's pointing stability must be improved more than tenfold. The simplest method to overcome this issue is to shorten the optical path for the probe laser pulse. We plan to shorten the current ~ 50 m of the optical path to ~ 5 m by introducing a single-pass amplifier, and the pointing stability is estimated to be suppressed by $\sim 1/10$.

ACKNOWLEDGMENTS

The work was supported by a Grant-in-Aid for Scientific Research (Japan Society for the Promotion of Science, Grants No. 20612024 and No. 23360045).

- [1] G. Materlik and T. Tshentscher, TESLA Technical Design Report, PART V (2001).
- [2] H.-D. Nuhn, Linac Coherent Light Source (LCLS) Conceptual Design Report No. SLAC-R-593, 2002.
- [3] J. Rivers, SCSS X-FEL Conceptual Design Report, RIKEN (2005).
- [4] O. H. Altemueller, R. R. Larsen, and G. A. Loew, *Rev. Sci. Instrum.* **35**, 438 (1964).
- [5] H. Ego and Y. Otake, in *Proceedings of the 11th European Particle Accelerator Conference, Genoa, 2008* (EPS-AG, Genoa, Italy, 2008), p. 1098.
- [6] X. Yan, A. M. MacLeod, W. A. Gillespie, G. M. H. Knippels, D. Oepts, A. F. G. van der Meer, and W. Seidel, *Phys. Rev. Lett.* **85**, 3404 (2000).
- [7] I. Wilke, A. M. MacLeod, W. A. Gillespie, G. Berden, G. M. H. Knippels, and A. F. G. van der Meer, *Phys. Rev. Lett.* **88**, 124801 (2002).
- [8] S. Casalbuoni, H. Schlarb, B. Schmidt, P. Schmuser, B. Steffen, and A. Winter, *Phys. Rev. ST Accel. Beams* **11**, 072802 (2008).
- [9] Y. Otake, H. Maesaka, S. Inoue, A. Higashiya, M. Yabashi, T. Shintake, K. Yanagida, H. Ego, and H. Tomizawa, in *Proceedings of the 11th European Particle Accelerator Conference, Genoa, 2008* (Ref. [5]), p. 1224.
- [10] H. Tomizawa, Japan Patent Application No. 2007-133046.
- [11] H. Tomizawa and M. Kobayashi, in *Proceedings of the 29th International Free Electron Laser Conference (FEL 07), Novosibirsk, Russia* (BINP, Novosibirsk, 2007), p. 382.
- [12] G. Berden, W. A. Gillespie, S. P. Jamison, E.-A. Knabbe, A. M. MacLeod, A. F. G. van der Meer, P. J. Phillips, H. Schlarb, B. Schmidt, P. Schmuser, and B. Steffen, *Phys. Rev. Lett.* **99**, 164801 (2007).
- [13] <http://refractiveindex.info>.
- [14] F. Pan, G. Knopfle, C. Bosshard, S. Follonier, R. Spreiter, M. S. Wong, and P. Gunter, *Appl. Phys. Lett.* **69**, 13 (1996).
- [15] X.-C. Zhang, X. F. Ma, Y. Jin, T.-M. Lu, E. P. Boden, P. D. Phelps, K. R. Stewart, and C. P. Yakymyshyn, *Appl. Phys. Lett.* **61**, 3080 (1992).
- [16] S. Matsubara, A. Maekawa, and H. Tomizawa, in *Proceedings of the 31st International Free Electron Laser Conference (FEL 09), Liverpool, UK* (STFC Daresbury Laboratory, Warrington, 2009), p. 269.
- [17] J. Dudley, G. Gentry, and S. Coen, *Rev. Mod. Phys.* **78**, 1135 (2006).
- [18] F. Verluise, V. Laude, Z. Cheng, C. Spielmann, and P. Tournais, *Opt. Lett.* **25**, 575 (2000).
- [19] S. C. Tidwell, D. H. Ford, and W. D. Kimura, *Appl. Opt.* **29**, 2234 (1990).
- [20] R. Yamaguchi, T. Nose, and S. Sato, *Jpn. J. Appl. Phys.* **28**, 1730 (1989).
- [21] M. Stalder and M. Schadt, *Opt. Lett.* **21**, 1948 (1996).
- [22] T. Hattori and T. Kobayashi, *Chem. Phys. Lett.* **133**, 230 (1987).
- [23] Y. Takahashi, H. Adachi, M. Takagi, Y. Hosokawa, S. Onzuka, S. Brahadeeswaran, M. Yoshimura, Y. Mori, H. Masuhara, T. Sasaki, and H. Nakanishi, *J. Photochem. Photobiol., A* **183**, 247 (2006).

-
- [24] M. G. Kuzyk and C. W. Dirk, [Appl. Phys. Lett.](#) **54**, 1628 (1989).
- [25] Y. Tanabe, *Macromolecular Science and Engineering : New Aspects* (Springer, New York, 1999).
- [26] P. Bolton (private communication).
- [27] LightTrans VirtualLab UG, Kahkaische Strasse 4, 07745, Jena, Germany.
- [28] J. W. Goodman, *Introduction to Fourier Optics* (Roberts and Company Publishers, Chicago, 2005).
- [29] H. Tomizawa, at the PMRC Colloquium, JAEA, Kyoto, Japan (2008).
- [30] H. Tomizawa, [Radiat. Phys. Chem.](#) **80**, 1145 (2011).
- [31] H. Minamide and K. Matsukawa (private communication).